Scilight

Regenerative Medicine and Dentistry
https://www.sciltp.com/journals/rmd



Article

Dual-Crosslinked Calcium Silicate/Alginate Hydrogel with Controlled Swelling Behavior for Enhanced Skin Wound Healing

Changlong Song [1,†], Dan Wan [1,†], Xincheng Huang [2], Qijun Du [3,4], Lu Tang [5], Suqi Wang [3,4,*] and Zhihong Dong [1,5,*]

[1] Department of Materials, School of Mechanical Engineering, Chengdu University, Chengdu 610106, China
[2] The Fourth People's Hospital, Chengdu 610031, China
[3] National Engineering Research Center for Biomaterials, Sichuan University, Chengdu 610065, China
[4] Tianfu Jincheng Laboratory, City of Future Medicine, Chengdu 641400, China
[5] Affiliated Hospital and Clinical College, Chengdu University, Chengdu 610106, China
* Correspondence: shuqi@scu.edu.cn (S.W.); zhdong@cdu.edu.cn (Z.D.)
† These authors contributed equally to this work.

How To Cite: Song, C.; Wan, D.; Huang, X.; et al. Dual-Crosslinked Calcium Silicate/Alginate Hydrogel with Controlled Swelling Behavior for Enhanced Skin Wound Healing. *Regenerative Medicine and Dentistry* **2026**, *3*(4), 17. https://doi.org/10.53941/rmd.2026.100017

Received: 9 August 2026
Revised: 11 November 2026
Accepted: 16 November 2026
Published: 20 November 2026

Abstract: Chronic cutaneous wounds require an extended healing period, thus imposing substantial psychological and financial burdens on patients. Sodium alginate (Alg) is widely used in biomedicine due to its excellent biocompatibility and cost-effectiveness. However, conventional Alg hydrogels exhibit excessive swelling because of their inherent hydrophilicity, which poses a risk of secondary injury. To address this issue, we developed a dual-crosslinked anti-swelling hydrogel. First, Alg was modified into methacryloylated alginate (AlgMA), which resulted in a 70% reduction in the equilibrium swelling ratio compared to Alg. Then, bioactive calcium silicate (CS) was incorporated to fabricate a composite hydrogel (CS/AlgMA). *In Vitro* studies showed that CS/AlgMA achieved a controlled swelling rate of 330%. Notably, the 20%-CS/AlgMA group demonstrated a sustained release of silicon/calcium ions. Biological assays confirmed that 20%-CS/AlgMA significantly promoted the proliferation and migration of human umbilical vein endothelial cells (HUVECs). These findings highlight CS/AlgMA as a promising approach for the long-term management of cutaneous wounds.

Keywords: wound repair; anti-swelling hydrogel; dual-crosslinking; sodium alginate; calcium silicate; bioactive ions

1. Introduction

The skin is the largest organ in the human body, accounting for approximately 15% of the body mass. It consists of the epidermis, dermis, subcutaneous tissue, and skin appendages [1,2]. As the body's first line of defense and constantly interacting with the external environment, the skin is made particularly vulnerable to environmental damage. When the skin's physical barrier function is impaired, pathogenic microorganisms can enter the body, potentially causing wound infections and, in severe cases, sepsis [3].

According to the healing duration, skin wounds can be categorized into two types: acute wounds and chronic wounds [4]. Acute wounds, which stem from accidental traumas or incisions, generally achieve spontaneous healing within a period ranging from days to weeks. Conversely, chronic wounds induced by burns, infections, or diabetes may endure for three months or more. Owing to their impaired self-healing ability, chronic wounds demand therapeutic interventions, such as medicated dressings [5–7]. Prolonged treatment not only incurs

Copyright: © 2026 by the authors. This is an open access article under the terms and conditions of the Creative Commons Attribution (CC BY) license (https://creativecommons.org/licenses/by/4.0/).
Publisher's Note: Scilight stays neutral with regard to jurisdictional claims in published maps and institutional affiliations.

significant medical costs but also subjects patients to continuous physical discomfort and psychological distress. Consequently, it is imperative to develop cost-effective dressings that can expedite the healing process and relieve the burden on patients.

Conventional sutures and staples induce secondary tissue damage, while bandages and gauze are increasingly obsolete due to poor biocompatibility and inability to provide a pro-healing microenvironment [8,9]. Hydrogels-particularly those based on the biocompatible, biodegradable, and low-cost like polysaccharide sodium alginate (Alg)-have emerged as preferred dressing materialst [10–12]. Their porous architecture resembling the native extracellular matrix (ECM) maintains a moist wound environment and can serve as a platform for cellular growth. For instance, He et al. [13] developed an alginate-based, dual-network hydrogel that forms a protective gel upon contact with wound exudate.

However, the widespread application of natural Alg hydrogels is constrained by two inherent limitations: hydrophilicity leading to excessive swelling, which risks wound re-rupture [14,15], and a general lack of bioactive signals to actively promote healing [16,17]. Therefore, an urgent need remains for engineered hydrogels that concurrently achieve anti-swelling performance and pro-healing functionality.

To address this challenge, we utilized calcium silicate (CS), a bioactive ceramic recognized for releasing therapeutic silicate ions [18,19]. These ions have exhibited remarkable pro-angiogenic ability by stimulating the proliferation, migration, and tube formation of human umbilical vein endothelial cells (HUVECs) [20–22]. Therefore, we hypothesized that integrating CS into an anti-swelling hydrogel would synergistically expedite wound healing via the combined effect of controlled swelling and sustained ion-mediated bioactivity.

This study addresses hydrogel swelling suppression. First, modified Alg with photo-crosslinkable methacrylic anhydride (MA) was synthesized to methacrylated alginate (AlgMA). AlgMA retains native complexing groups (–COO^-) while introducing photo-polymerizable moieties, enabling dual-crosslinking to achieve high crosslinking density and consequent anti-swelling efficacy.

Subsequently, CS was integrated with AlgMA to fabricate anti-swelling composite hydrogels (CS/AlgMA) (Scheme 1). The physicochemical properties, including surface morphology, mechanical strength, swelling behavior, and ion release kinetics, were systematically characterized.

Furthermore, the therapeutic potential of CS/AlgMA hydrogels was evaluated using HUVECs *in vitro* and *in vivo* through animal experiments.

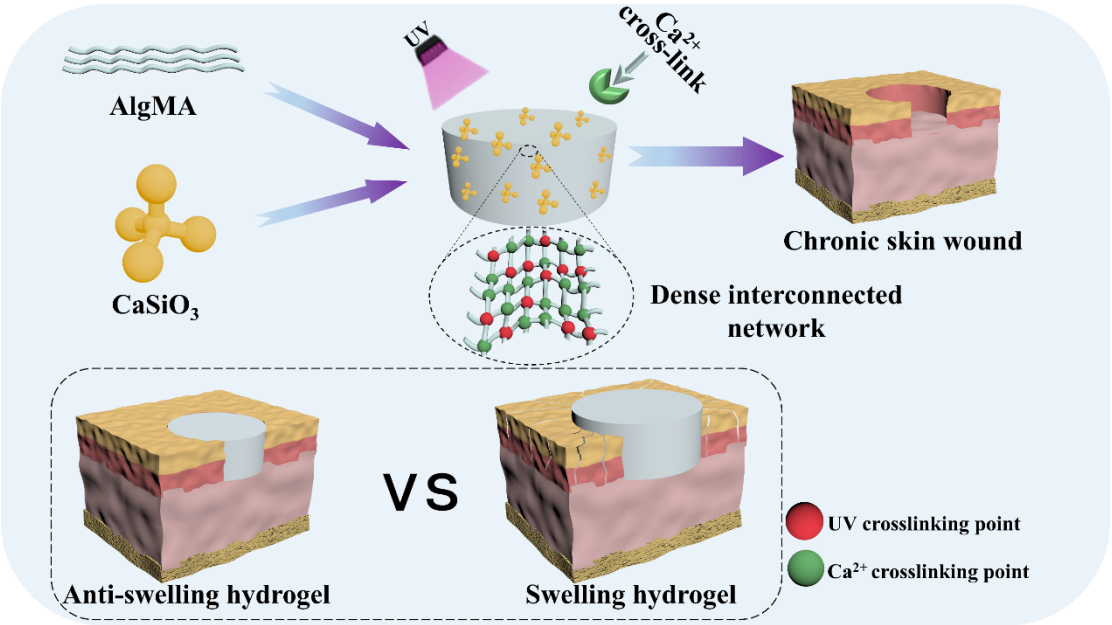

Scheme 1. An anti-swelling CS/AlgMA hydrogel by Chemical Crosslinking (UV) and Ionic Crosslinking (Ca^{2+}) for skin wounds healing.

2. Materials and Methods

2.1. Materials

Sodium alginate (viscosity 200 ± 20 mpa·s), methacrylic anhydride (Mw 154.16 g/mol), calcium silicate ($CaSiO_3$), anhydrous calcium chloride ($CaCl_2$), and other chemicals used in the study were purchased from Aladdin (Shanghai, China). Dialysis bags (MWCO: 8000–14,000 Da; Product No. MD77) were purchased from Jellop (CA,

USA). Lithium Phenyl (2,4,6-trimethylbenzoyl) phosphate (LAP) and Cell Counting Kit-8 (CCK-8) were sourced from Shanghai Yuanye Biotechnology Co., Ltd. and Asen Biotechnology (Shanghai, China) Co., Ltd., respectively.

2.2. Synthesis and Structural Characterization of AlgMA

Sodium alginate (Alg) is a linear polysaccharide composed of β-1,4-linked guluronic acid (G-block) and mannuronic acid (M-block) residues (Figure S1a) [23]. The presence of hydroxyl and carboxyl groups on each monosaccharide unit enables chemical modification. Sodium methacryloylated alginate (AlgMA) (Figure S1b) was synthesized following established methods [24]. Briefly, 2 g of sodium alginate was dissolved in 300 mL deionized water, and the pH was adjusted to 8.0–9.0 with 4 mL of 4 M NaOH. Methacrylic anhydride (15 mL) was added dropwise (1 mL/min) to the solution under continuous pH maintenance (8.0–9.0) using 4 M NaOH. The reaction proceeded for 24 h at 23 °C. The resultant mixture was centrifuged (5000 rpm, 15 min), and the supernatant was dialyzed (MWCO: 8–14 kDa) against deionized water for 7 days with water changes thrice daily under agitation (300 rpm). The dialysate was freeze-dried at −20 °C for 24 h, followed by lyophilization (−80 °C, 72 h) to obtain AlgMA.

^{1}H NMR spectroscopy: AlgMA (5 mg) was dissolved in D_2O (1 mL) and analyzed by NMR to confirm methacrylation; FTIR spectroscopy: Fourier-transform infrared spectra of AlgMA powder were acquired to identify characteristic functional groups.

2.3. Preparation of CS/AlgMA Hydrogels

Hydrogels with varying calcium silicate (CS) concentrations (0, 10, 20, and 40 wt%) were fabricated via solution casting and dual-crosslinking. Specifically: 0, 0.02, 0.04, or 0.08 g of CS was ultrasonically dispersed (300 W, 40 kHz) in 10 mL deionized water at 50 °C for 15 min. Then 0.02 g LAP was added to the suspension under light-protected conditions and stirred for 30 min. Next 0.2 g AlgMA was introduced and mixed for 6 h under light avoidance. The mixture was heated to 55 °C in a water bath, cooled to 25 °C, and degassed via vacuum cycling (0.1 MPa, 3 cycles). After that the solution was injected into cylindrical molds (Ø10 × 1 mm), then UV-cured (365 nm, 15 s). Finally, resulting hydrogels were immersed in 0.6% (w/v) $CaCl_2$ solution for 24 h to ionic crosslinking, then frozen at −80 °C, lyophilized, and vacuum-sealed.

2.4. Physicochemical Characterization of CS/AlgMA Hydrogels

Surface morphology of hydrogel was analyzed by Scanning Electron Microscope (SEM). Hydrogel samples were mounted on aluminum stubs with conductive carbon tape, sputter-coated with 15-nm gold/palladium (15 mA, 60 s), and imaged at 10 kV accelerating voltage under high vacuum (10^{-3} Pa). Molecular bonding of crosslinking hydrogel was analyzed by Fourier Transform infrared spectroscopy (FTIR). Hydrogels (2–3 mg) were lyophilized, mixed with KBr (1:100 ratio), and pressed into transparent pellets. Spectra were acquired in transmission mode (400–4000 cm^{-1}, 4 cm^{-1} resolution, 32 scans).

Further hydrophilicity of hydrogel was evaluated, Lyophilized hydrogels were compressed into films (1 mm thickness). Static water contact angles were measured at 25 °C using 2 μL deionized water droplets (n = 5 per group). The swelling ratio of hydrogel was evaluated, special processing as followed, pre-weighed dry hydrogels (W_0) were immersed in PBS (pH 7.4, 25 °C). At predetermined intervals (1, 3, 5, 7, 10, 14, 21 h), samples were removed from the PBS, the surface water was carefully blotted with filter paper, and the wet weight (W_t) was immediately recorded. The swelling ratio (Q) at each time point was calculated using the following equation, $Q\ (\%) = [(W_t - W_0)/W_0] \times 100$. The experiment was continued until the samples reached swelling equilibrium (constant weight).

In Vitro degradation was evaluated. Pre-weighed hydrogels (W_i) were incubated in SBF (50 mL, pH 7.4) at 37 °C with agitation (100 rpm). On Day 1, 3, 5, 7, 14, 21, 28, samples were rinsed (DI water ×3, ethanol ×3), lyophilized, and weighed (W_d). SBF refreshed every 3 days. Degradation rate (P%) was calculated as: $P\ (\%) = [(W_i - W_d)/W_i] \times 100$. Further calcium, silicate ion concentrations were quantified by ICP-MS (calibration range: 0.01–100 ppm).

Dumbbell-shaped specimens (Type V, ASTM D638) were fabricated as in Section 2.3 for mechanical testing [25]. Tensile tests were performed at 1 mm/min until failure (0.5 N preload. Young's modulus (E), ultimate tensile strength (UTS), and elongation at break (ε) were calculated.

2.5. In Vitro Biological Characterization

HUVECs (Thermo Fisher, Waltham, MA, USA) cultured in Endothelial Cell Medium (ECM) and 5% fetal bovine serum (FBS) and 1% endothelial cell growth supplement (ECGS) and 1% penicillin/streptomycin solution (P/S). All cells maintained at 37 °C/5% CO_2 with medium changes every 48 h.

Hydrogels were sterilized by 75% ethanol for 2 h and UV irradiation for 30 min/side and finally PBS washing 3 times. Conditioned medium was prepared by incubating the hydrogels in serum-free medium at a ratio of 0.1 g hydrogel per mL medium for 24 h at 37 °C. The extracts were then collected and filtered through a 0.22 μm filter. For cell experiments, the extracts were used at 50% concentration. Cells were seeded in 48-well plates (HUVECs: 2×10^4/well), exposed to conditioned media for 72 h, then stained with calcein-AM/PI (15 μg/mL each, 30 min). Viability was quantified via fluorescence microscopy (n = 5). At days 1, 3, 5, CCK-8 reagent (10% v/v in medium) was added to evaluate the cell proliferation. After 2 h incubation, absorbance was measured at 450 nm (reference: 650 nm).

Confluent monolayers in 6-well plates were scratched with 200-μL pipette tips to evaluate the cell migration. After PBS washing, hydrogel extracts were added. Scratch closure was monitored at 0/12/24/48 h using phase-contrast microscopy. Migration rate was calculated as: Migration (%) = $[(A_0 - A_t)/A_0] \times 100$. where A_0: initial scratch area, A_t: area at time t.

2.6. In Vivo Zoological Characterization

Effect of CS/AlgMA on Wound Healing *In Vivo*

Animal experiments were approved by the Institutional Animal Care and Use Committee (IACUC) of West China Hospital, Sichuan University (Protocol 20250422006) in compliance with NIH guidelines. Full-thickness skin wounds (10 mm diameter) were created on the dorsum of ICR mice (6-week-old, ~40 g, SPF-grade) to model acute wound healing. Mice were randomized into three groups (n = 5/group), Untreated Control, AlgMA, and 20%-CS/AlgMA, respectively.

The surgical procedure was performed following a standardized protocol. After a 12 h fasting period, anesthesia was induced in the animals via intraperitoneal injection of sodium pentobarbital (40 mg/kg). Using a depilatory cream, the dorsal hair was then removed by electric clipping for 4–5 min, after which the surgical site was disinfected with 75% ethanol. Full-thickness skin wounds were created by a sterile biopsy punch, Then, 300 μL of the corresponding hydrogel precursor solution was applied evenly to the wound bed and crosslinked (with the control group receiving no treatment). Finally, the animals were placed on a warming pad maintained at 37 °C for postoperative recovery.

Wound closure was monitored by standardized photography on 0, 7, and 14 day. Post-operation, and the wound areas were quantified using ImageJ software (version 1.54t). At the corresponding time points (days 7 and 14), the animals were euthanized, and the wound tissues were harvested and immediately fixed in 4% paraformaldehyde (PFA) for subsequent histological analysis.

The fixed tissues were paraffin-embedded and sectioned at 5 μm thickness for subsequent histological analyses. Hematoxylin and eosin (H&E) staining was performed using a commercial kit (Sigma-Aldrich, St. Louis, MO, USA) to evaluate neo-tissue formation and inflammatory responses. Masson's trichrome staining was applied to assess collagen deposition, with the area of collagen-positive signals quantified using Image-Pro Plus 6.0 software. For immunohistochemical staining, sections underwent antigen retrieval and then incubated with primary Anti-CD31 (ab182981, Abcam) to quantify microvessel density, and antibody Anti-Ki67 (HA721115, HUABIO) to determine the proliferation index (expressed as percentage of positive cells).

2.7. Statistical Analysis

The statistical analyses were conducted using GraphPad Prism 8 software. All results are expressed as the mean ± standard deviation. One-way ANOVA was used for single-time-point data, while two-way ANOVA was used for multi-time-point/two-factor data; Tukey's post hoc test was used for all multiple comparisons. The statistical significance was denoted as * $p < 0.05$, ** $p < 0.01$, and *** $p < 0.001$.

3. Results and Discussion

3.1. AlgMA Synthesis and Characterization

AlgMA was synthesized via methacrylic anhydride substitution onto alginate hydroxyl groups. Successful functionalization was confirmed by FTIR and ^{1}H-NMR. In Figure 1a, FTIR demonstrated the emergence of C=O stretch peak at 1724 cm^{-1} [26]. In Figure S2, ^{1}H-NMR verified characteristic methacrylate proton peaks at 1.8,

5.6, and 6.1 ppm [27]. These results showed that the dual-crosslinked AlgMA hydrogel exhibited superior anti-swelling performance and mechanical strength compared with the single-crosslinked Alg hydrogel, which was crosslinked solely by Ca^{2+} ionic interactions. Figure 1b,c showed 70% lower equilibrium swelling ratio, while Figures 1d and S3 showed 2 MPa higher tensile strength at rupture. These results indicated that the improved swelling resistance of the dual-crosslinked AlgMA hydrogel arises from the combined effects of ionic and covalent crosslinking. Ionic crosslinking alone, formed between Ca^{2+} and alginate G blocks, creates a reversible "egg-box" physical network that restricts chain mobility but is prone to ion exchange and dissociation in aqueous media, resulting in limited swelling resistance. While UV-induced covalent crosslinking alone, formed by free-radical polymerization of methacrylate groups, creates a permanent network with reduced mesh size, but its crosslinking density is limited by the degree of methacrylation and it lacks an efficient energy-dissipation mechanism. So in the dual-crosslinked system, the ionic crosslinks act as sacrificial bonds that dissipate energy and distribute stress, while the covalent crosslinks fix the network and prevent dissociation of the ionic crosslinks. This synergy leads to a higher total crosslinking density, a smaller mesh size, and a more stable network, thereby markedly reducing water penetration and swelling while maintaining mechanical integrity [28].

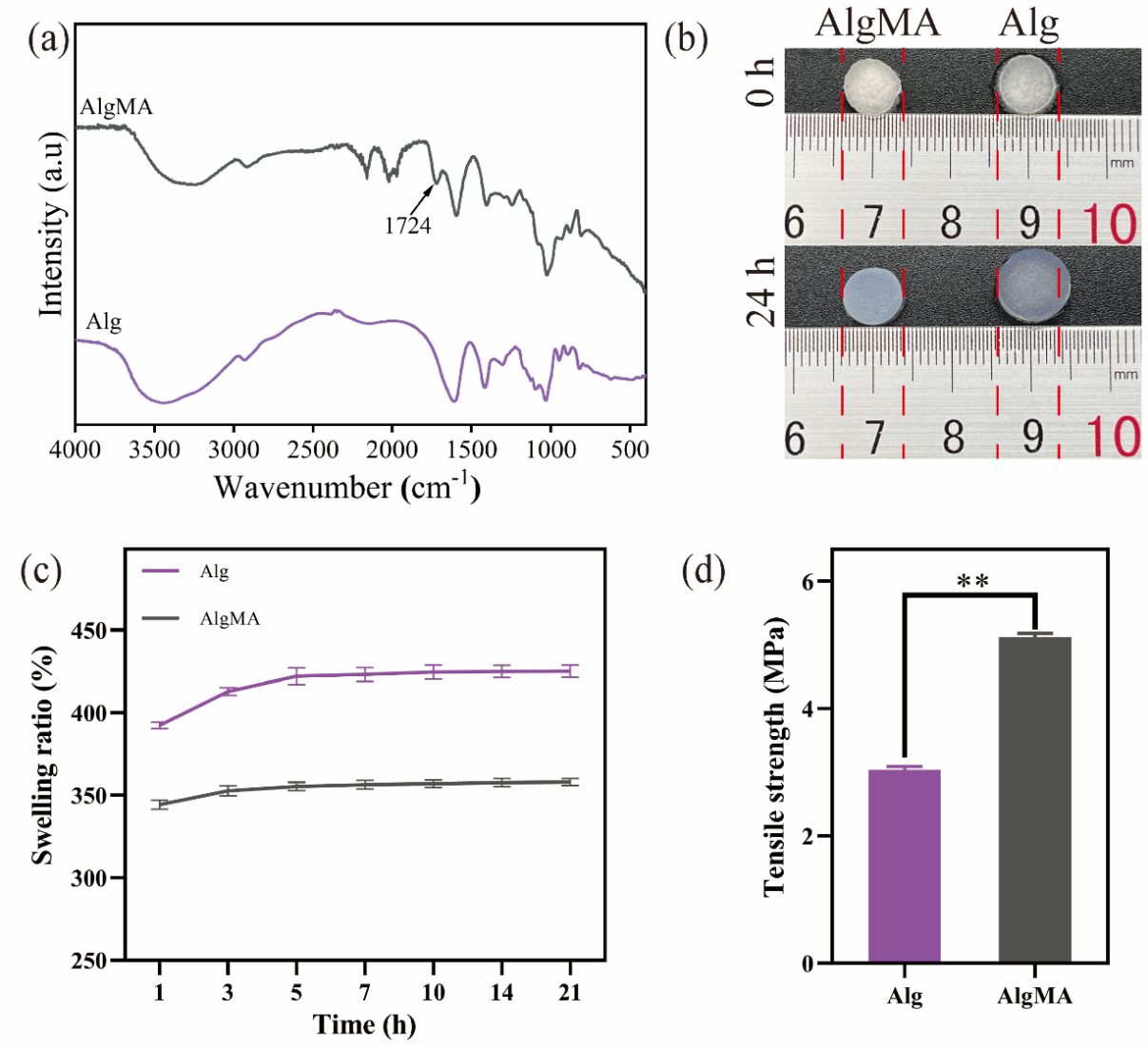

Figure 1. Characterization of alginate (Alg) modification. (**a**) FTIR spectra; (**b**) Swelling visualization; (**c**) Swelling ratio quantification (n = 3); (**d**) Tensile modulus (n = 5). ** $p < 0.01$.

3.2. Physicochemical Characterization of CS/AlgMA Hydrogels

The morphology of CS/AlgMA hydrogels after dual-crosslinking is shown in Figure 2a. Following UV crosslinking, the hydrogels maintained structural integrity within molds. A visible color transition from transparent to opaque was observed with increasing CS content (0 → 40 wt%). Subsequent Ca^{2+} ionic crosslinking induced significant volumetric contraction, confirming successful secondary crosslinking.

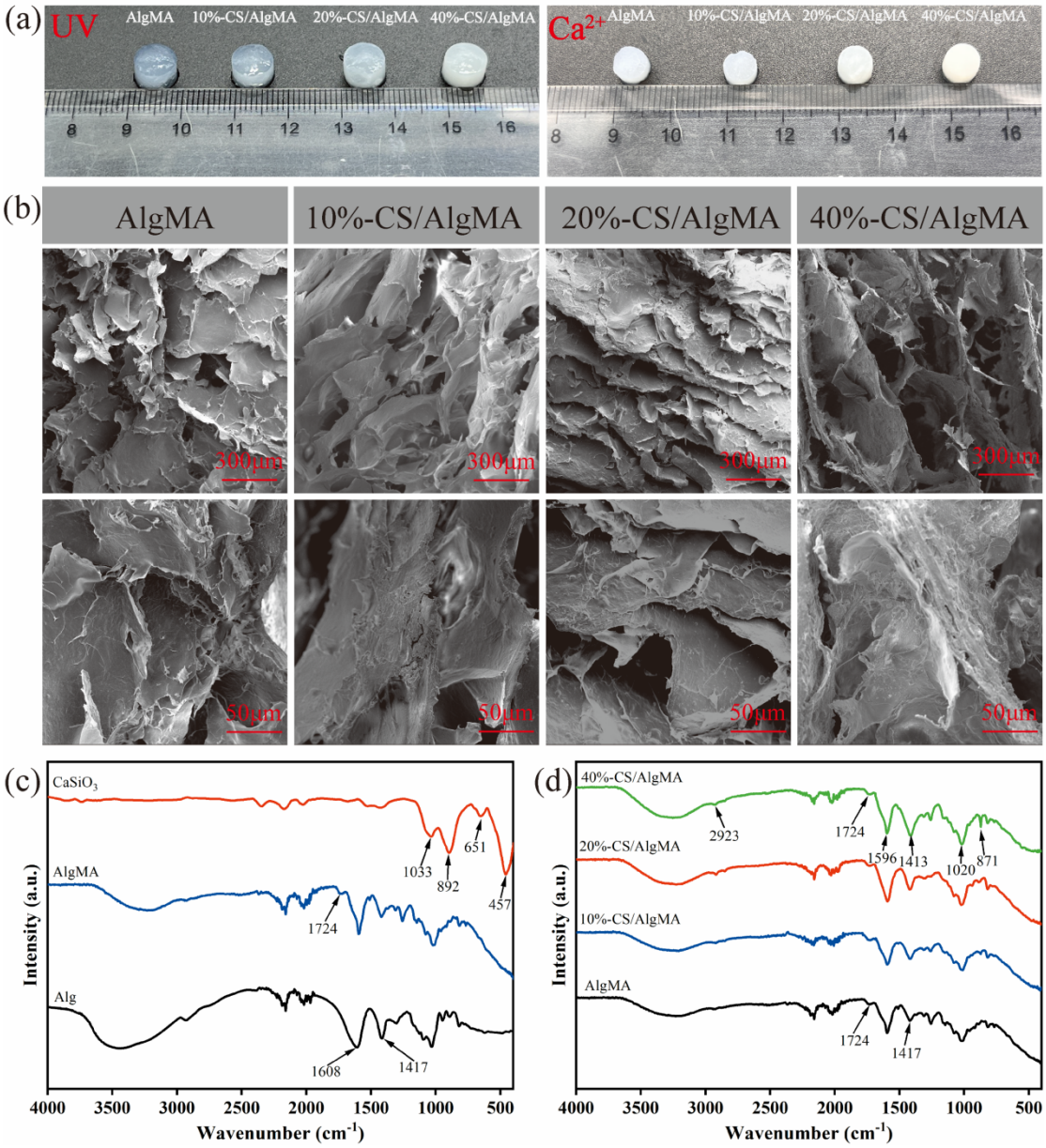

Figure 2. (**a**) Macroscopic view of CS/AlgMA with UV and Ca^{2+} crosslinking; (**b**) CS/AlgMA surface morphology by SEM; (**c**,**d**) FTIR of CS, Alg, AlgMA and CS/AlgMA.

SEM of lyophilized samples (Figure 2b) revealed that all compositions retained a three-dimensional porous network. Notably, higher CS loading promoted the attachment of silicate particles along pore ridges. These interconnected microchannels facilitate nutrient/oxygen transport while providing topological cues for cell adhesion and migration [29]. At 40 wt% CS concentration, homogeneous distribution of silicon throughout the matrix indicated effective complexation between CS and the AlgMA network.

FTIR is an excellent technique for validating interactions between material components and examining their binding states by detecting changes in functional groups [30]. Therefore, FTIR was employed to characterize the raw materials. The results are displayed in Figure 2c: peaks at 1033 cm^{-1} correspond to Si-O bond stretching vibrations; peaks at 892 cm^{-1} are attributed to Si-O-Si bonds; peaks at 651 cm^{-1} indicate Ca-O bond stretching vibrations; and peaks at 457 cm^{-1} signify O-Si-O bond bending vibrations. The characteristic peak at 1724 cm^{-1} is attributed to the C=O stretching vibration of the ester carbonyl in the methacrylate groups introduced by methacrylic anhydride (MA) during AlgMA synthesis, while peaks at 1608 cm^{-1} and 1417 cm^{-1} represent the asymmetric and symmetric stretching vibrations of the –COOH group in alginate (Alg), respectively.

Following cross-linking within the composite material, the distinctive peaks of each component remain evident (Figure 2d). Furthermore, the peak of 40% CS/AlgMA at 871 cm^{-1} suggested an interfacial interaction between CS and AlgMA that perturbs the Si-O (non-bridging oxygen) or Si-O-Ca vibrational environment. Additionally, these peak intensities increase with higher CS content. The signal at 2923 cm^{-1} corresponds to C-H

bonds within the composite molecular chain, indicating the formation of hydrogen bonds in the molecular network post-cross-linking. The characteristic C=O peak from MA persists at 1724 cm^{-1}, suggesting that the cross-linking process did not disrupt the molecular structure of the original AlgMA. Shifts in peak positions and intensities at 1596 cm^{-1} and 1413 cm^{-1} were observed, resulting from the red-shift of the –COOH vibrations induced by cross-linking with Ca^{2+} ions. This red-shift is attributed to the formation of complexes between the polysaccharide's carboxyl groups and calcium ions [31].

3.3. Multidimensional Analysis: Hydrophilicity, Ion Release, Mechanical-Swelling-Degradation Properties

Surface hydrophilicity critically regulates cell behavior-including attachment, proliferation, differentiation, and biocompatibility [32]. As evidenced by contact angle measurements (Figures 3a and S4), CS/AlgMA composites exhibited reduced hydrophilicity versus AlgMA controls ($p < 0.01$), likely due to changes in surface chemistry and/or surface roughness introduced by CS. Notably, even at 40% CS loading, the contact angle remained 61.3 ± 1.02° (** $p < 0.01$), confirming sustained hydrophilicity (θ < 90°).

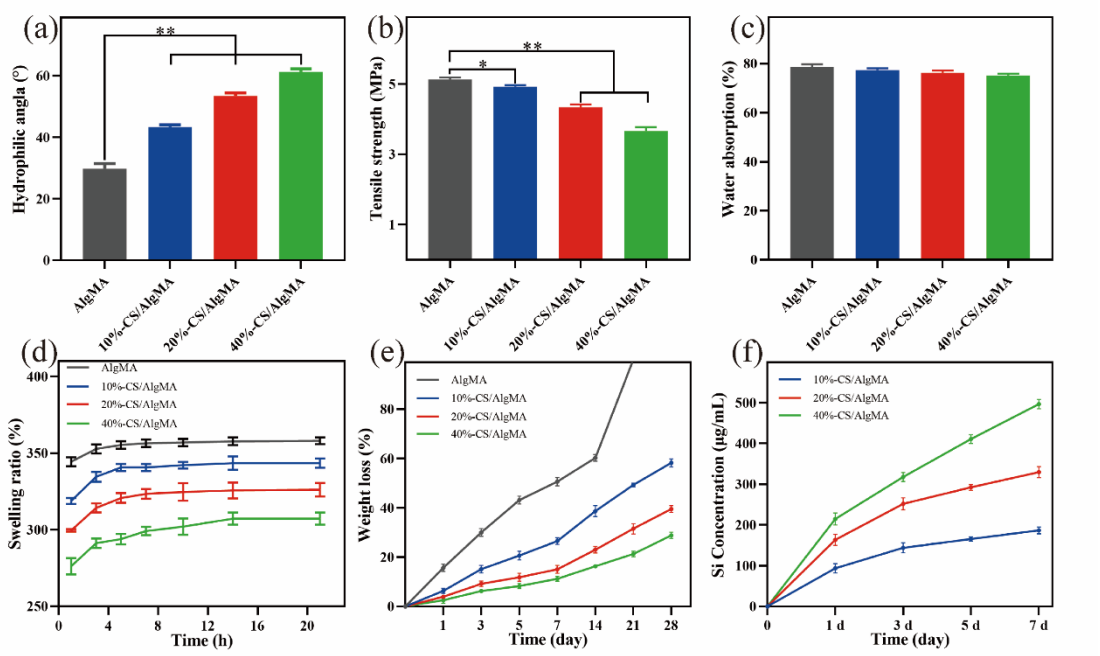

Figure 3. Physicochemical properties of CS/AlgMA composites. (**a**) Water contact angle; (**b**) Tensile strength; (**c**) Water content; (**d**) Swelling ratio; (**e**) *In Vitro* degradation; (**f**) Si release profile. * (Data expressed as mean ± SD, n = 3 for a, c, d, e, f; n = 5 for b. * $p < 0.05$, ** $p < 0.01$).

Tensile testing of hydrogel composites (Figures 3b and S5) demonstrated decreasing tensile strength with increasing CS content, suggesting structural disruption by CS incorporation. Despite this trend, the 20% CS/AlgMA formulation maintained a tensile strength of 4.3 ± 0.11 MPa (** $p < 0.01$), exceeding the stress threshold for skin tissue applications [33]. This confirms that optimized CS loading achieves to better mechanical performance.

Hydrogels immersed in PBS reached swelling equilibrium within 12 h, with rapid absorption occurring within 3 h (Figure 3d). Swelling ratios decreased significantly with higher CS content, as followed AlgMA was 357.98 ± 2.48%, 10% CS was 343.46 ± 3.46%, 20% CS was 326.03 ± 4.93% and 40% CS was 306.41 ± 4.00% ($p < 0.05$ vs. AlgMA), the equilibrium water content remained similarly 80% water content (Figure 3c). This indicates that the incorporation of CS primarily serves to restrict excessive network expansion and water uptake (i.e., anti-swelling), without compromising the intrinsic hydration capacity of the hydrogel matrix. The preserved high water content is essential for maintaining a moist environment to promote wound healing.

Under 28-day simulated physiological conditions, degradation analysis confirms that CS/AlgMA composites exhibited controllable degradation (Figure 3e). AlgMA degraded completely by 21 days, which was unsuitable for chronic wounds. Increasing CS content significantly slowed degradation ($p < 0.01$), mass loss was as followed by 28 days:10% CS was 58.23 ± 1.44%, 20% CS was 39.48 ± 1.48% and 40% CS was 28.84 ± 1.39%, respectively. So the degradation kinetics of 20% CS/AlgMA were controlled by optimal CS content, which may maintain wound-bridging integrity, enable sustained bioactive ion release and promote progressive scaffold resorption, thereby matching the kinetics of tissue regeneration [33].

Corresponding ion release kinetics demonstrated the positive correlation between CS content and Si and Ca ions release concentrations (Figures 3f and S6). The release exhibited a biphasic pattern: an initial burst release within the first 24 h, likely due to the rapid release of ions from the surface and near-surface of the hydrogel, followed by a sustained and controlled release over the subsequent 7 days. This sustained phase is attributed to the gradual degradation of the hydrogel matrix and the diffusion of ions from the inner core. As expected, the cumulative amount of released Si and Ca ions was directly proportional to the initial CS content, with the 40%-CS/AlgMA group showing the highest concentration. This controlled and sustained ion release profile creates a persistent bioactive ionic microenvironment for wound healing, which is considered beneficial for maintaining long-term bioactivity.

Based on the comprehensive evaluation of mechanical properties, swelling behavior, degradation rate, and ion release profiles, the 20%-CS/AlgMA formulation was identified as the optimal composition, offering a balanced combination of structural stability and bioactive ion release for subsequent biological assays.

3.4. In Vitro Biological Evaluation

To evaluate the biocompatibility and bioactivity of the CS/AlgMA hydrogels, a series of assays were conducted using HUVECs. The assessments focused on cytotoxicity, proliferative capacity, viability, and migratory behavior, which are critical indicators for wound healing applications [34].

3.4.1. CS/AlgMA Promotes HUVECs Proliferation and Viability

It was investigated that the potential cytotoxic effects of CS/AlgMA extracts on HUVECs, as endothelial cell viability is paramount for angiogenesis. Live/dead staining (Figure 4a) after 5 days of culture revealed a predominantly green fluorescence signal across all groups, indicating a high proportion of viable cells. Notably, the 20%-CS/AlgMA group exhibited a denser population of viable cells compared to the control and other CS-containing groups, suggesting an enhanced cytocompatibility.

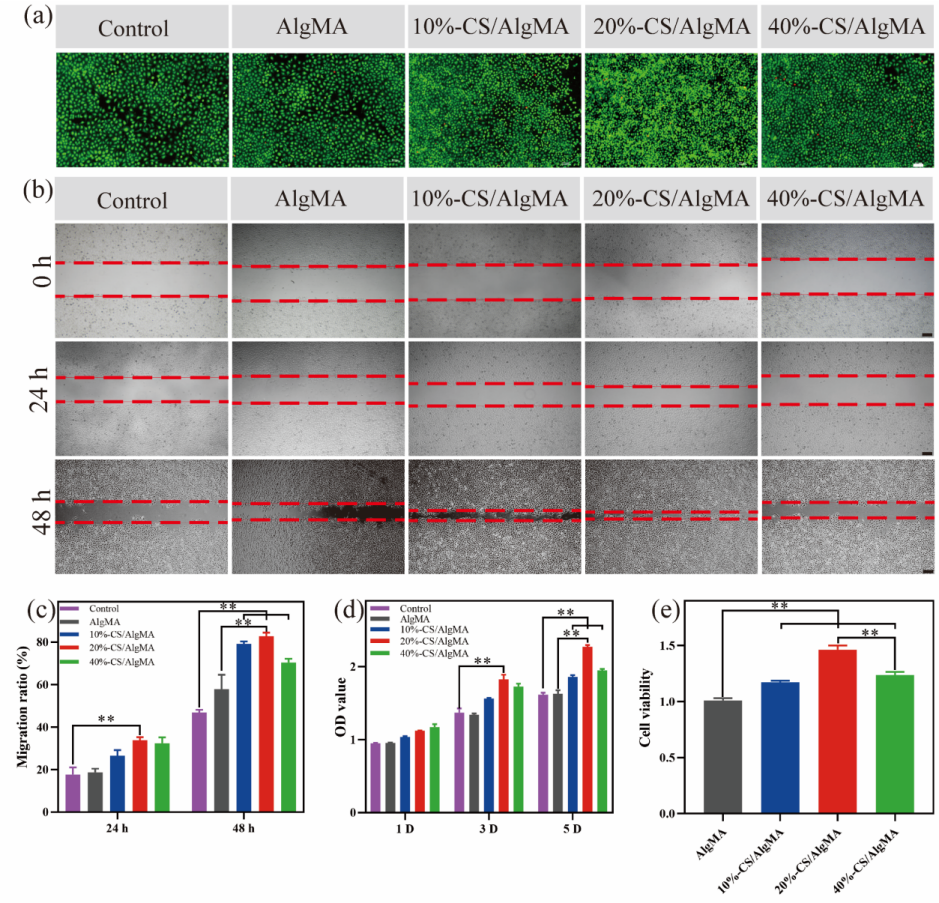

Figure 4. CS/AlgMA promotes HUVECs functions. (**a**) Viability staining (AM/PI, n = 5); (**b**) Scratch assay migration (24/48 h, n = 5); (**c**) Quantitative migration rate (48 h, n = 5); (**d**) Proliferation (CCK-8, 1/3/5 d, n = 5); (**e**) Cell viability quantification (n = 5). ** $p < 0.01$ vs control; Scale bars: 100 μm (**a**,**b**).

To quantitatively assess cell proliferation, a CCK-8 assay was performed over 5 days (Figure 4d,e). The results demonstrated a time-dependent increase in cell viability across all groups. Importantly, HUVECs cultured with 20%-CS/AlgMA extracts showed a significantly higher metabolic activity at day 3 and day 5 compared to other groups ($p < 0.01$), underscoring the superior capacity of this formulation to stimulate endothelial cell proliferation. Notably, the 40%-CS/AlgMA group showed lower HUVEC viability than the 20%-CS/AlgMA group, consistent with previous reports that high concentrations of silicate ions can inhibit endothelial cell viability.

3.4.2. CS/AlgMA Enhances the Migratory Capacity of HUVECs

Cell migration is a crucial step in angiogenesis during wound healing. Therefore, the next test evaluated the influence of CS/AlgMA on HUVECs motility using a scratch assay (Figure 4b,c and Table S1). After 48 h of incubation, all CS-containing groups demonstrated significantly enhanced wound closure rates compared to the control group. Among them, the 20%-CS/AlgMA group achieved the highest migration rate (82.83 ± 1.73%, $p < 0.01$), indicating its potent effect in promoting endothelial cell migration.

3.5. In Vivo Wound Regeneration Evaluation

Full-thickness skin defects (Ø10 mm) were established to an acute wounds model as an initial evaluation of the wound-healing efficacy at 0, 7, and 14 days post-treatment. As shown in Figure 5a, by Day 7, scab formation occurred universally, but the 20%-CS/AlgMA group showed superior regenerative capacity with nascent tissue formation around the scab. By Day 14, the control group still had persistent exudate, while the AlgMA group had none due to high water absorption. Critically, the 20%-CS/AlgMA group achieved near-complete epithelialization (96.0 ± 0.51%) with minimal infection or suppuration, attributed to anti-swelling properties, and nearly complete wound closure with smooth neoepidermis regeneration, significantly outperforming control (89.5 ± 1.2%) and AlgMA (93.5 ± 1.0%) groups ($p < 0.01$, Figure 5b,c).

Histopathological analysis of wound tissues on Day 7 (H&E staining; Figure 5d) revealed distinct outcomes across experimental groups. Control group exhibited extensive tissue necrosis accompanied by dense inflammatory infiltration. In contrast, AlgMA hydrogel showed only marginal epidermal thickening without significant inflammation. Notably, 20%-CS/AlgMA composite group demonstrated accelerated re-epithelialization, in which a continuous neo-epidermis covered most of the wound bed, together with markedly reduced inflammatory infiltration.

By Day 14, H&E staining further demonstrated a marked divergence in wound healing progression. Control group wounds displayed persistent chronic inflammation accompanied by pronounced fibrotic deposition, indicating impaired tissue regeneration. In stark contrast, 20%-CS/AlgMA group exhibited complete formation of a stratified, mature epidermis with restored dermal-epidermal junction integrity, alongside minimal to absent inflammatory infiltration.

Masson's trichrome staining (Figure 5e) highlighted collagen deposition (blue) versus immature fibrous tissue (red). At Day 7, the control group had abundant disorganized red fibers, while treatment groups had increased mature collagen (blue arrows). Quantitative analysis (Figure 5f, Table S2) confirmed that the 20%-CS/AlgMA group had the highest collagen deposition (20.46 ± 5.53%), surpassing the Control and AlgMA groups. By Day 14, all groups showed elevated collagen content, with the 20%-CS/AlgMA group achieving the most significant increase (~27%), demonstrating its robust capacity to stimulate structured dermal regeneration.

3.6. Neovascularization and Cellular Proliferation

CD31 Immunostaining (Figure 6a,b) showed that at Day 7, 20%-CS/AlgMA exhibited an increase of 85% microvessel density vs. control ($p < 0.01$), with dense $CD31^+$ microvessels (arrows) versus sparse distribution in controls. This pro-angiogenic advantage persisted at Day 14, where 20%-CS/AlgMA maintained 1.8-fold higher vessel counts ($p < 0.001$). These results confirmed that sustained vascular regeneration is critical for nutrient/O_2 delivery.

The Ki67 index revealed significant temporal enhancement in the 20%-CS/AlgMA group versus control (Figure 6c,d). At Day 7, the control group showed a value of 1.02 ± 0.31%, while the 20%-CS/AlgMA group had a value of 2.87 ± 0.42% ($p < 0.05$ compared with the control group), representing an 181% proliferative activation ($p < 0.05$). Despite the overall suppression of inflammation at this time, the number of $Ki67^+$ cells still increased in the 20%-CS/AlgMA group. At Day 14, the control group had a value of 2.10 ± 0.58%, and the 20%-CS/AlgMA group reached 5.25 ± 1.39% ($p < 0.01$ compared with the control group), indicating a 150% increase in proliferation. Moreover, cell proliferation peaked at this time (5.25%), synchronizing temporally with the near-complete wound closure.

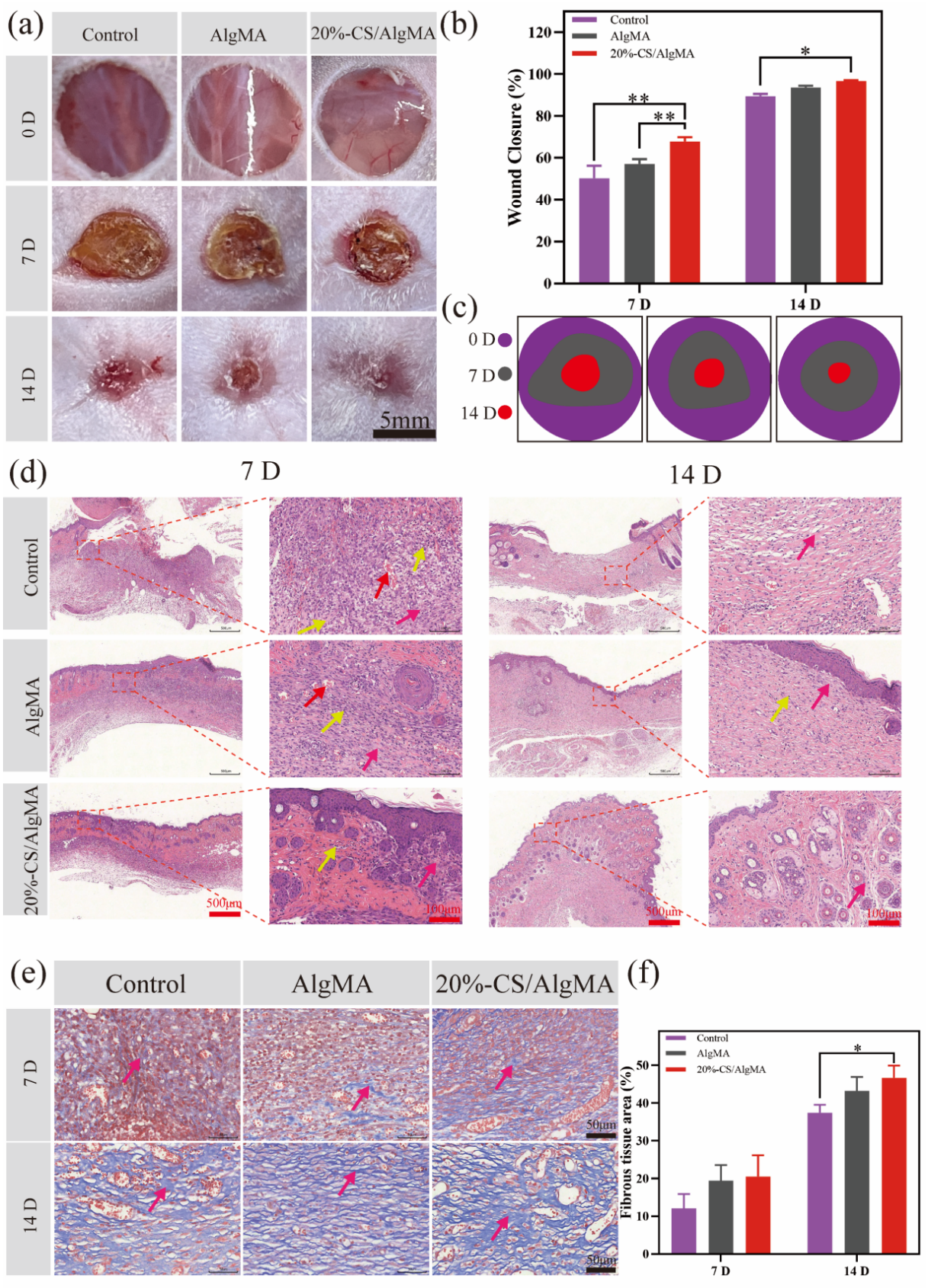

Figure 5. Wound healing progression with CS/AlgMA treatment (**a**) Macroscopic wound appearance; (**b**) Closure rate quantification (7/14 d, n = 5); (**c**) Healing trajectory analysis; (**d**) H&E staining (inflammatory response); (**e**) Masson's trichrome (collagen deposition); (**f**) Collagen deposition quantification (n = 5). * $p < 0.05$, ** $p < 0.01$ vs. control.

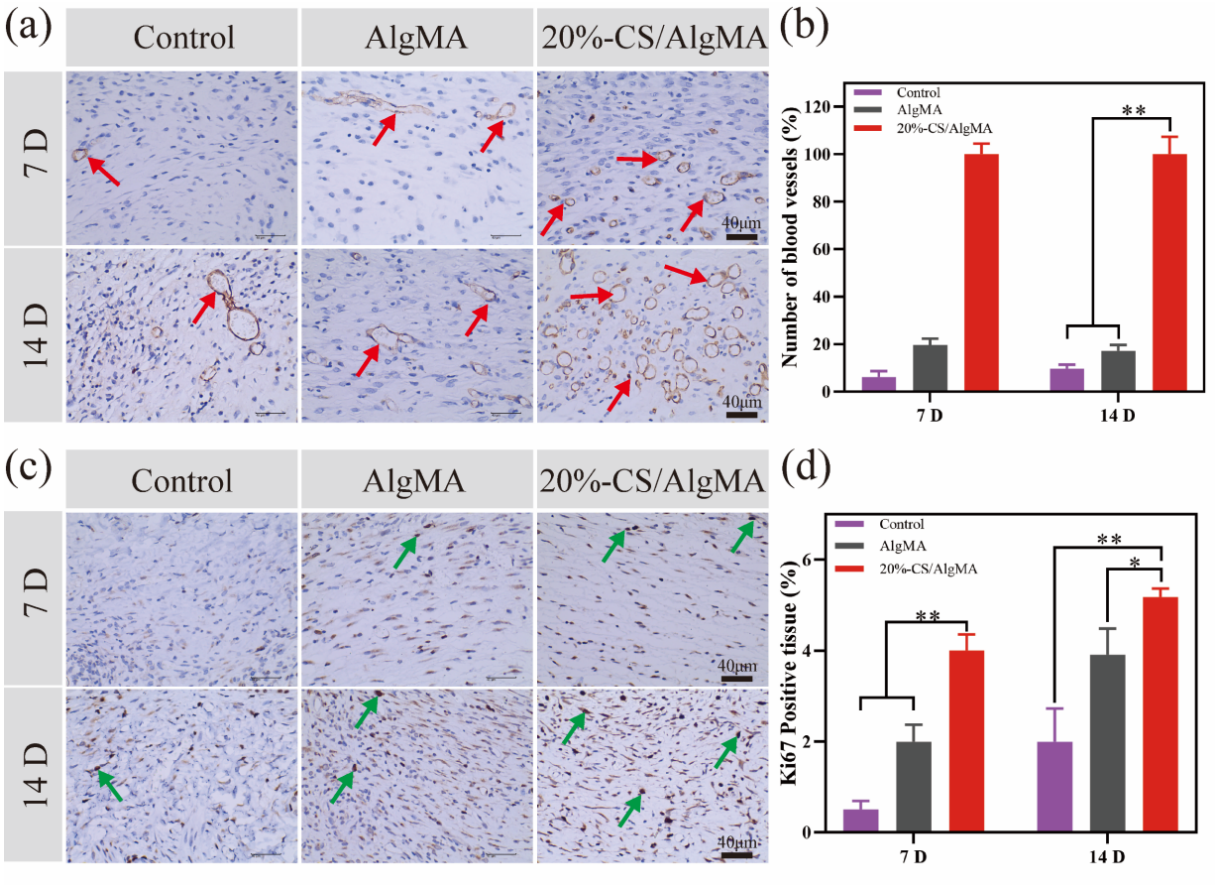

Figure 6. Enhanced angiogenesis and cellular proliferation. (**a**) $CD31^+$ microvessels (IHC, red arrows); (**b**) Neovessel density quantification (n = 5); (**c**) $Ki67^+$ proliferating cells (IHC, green arrows); (**d**) Proliferation index quantification (n = 5). * $p < 0.05$, ** $p < 0.01$ vs. control.

The management of skin wounds demands cost-effective therapies that mitigate pain while accelerating healing [35,36]. Conventional gauze dressings require frequent changes (typically every 3 days), posing risks of secondary injury due to tissue adhesion [37]. Naturally derived polymers like alginate offer advantages through their biomimetic extracellular matrix (ECM) structure, biocompatibility, and accessibility [38,39]. Herein, an anti-swelling composite hydrogel (CS/AlgMA) by functionalizing alginate with methacrylate groups (AlgMA) and incorporating bioactive calcium silicate (CS) demonstrated exceptional anti-swelling properties (equilibrium swelling ratio: ~330% vs. >800% in benchmark hydrogels [13]), sustained silicate ion release (>7 days, Figures 3f and S6) and controlled biodegradation (39.48 ± 1.48% mass loss at 28 days). Based on this degradation trend, the hydrogel may have the potential to support tissue repair over an extended period, consistent with similar degradation profiles reported in the literature [40,41]. Yet longer-term degradation studies and extended wound treatment experiments are needed to evaluate the functional lifetime of the hydrogel for tissue repair [42].

Critically, CS/AlgMA synergistically addresses two fundamental challenges in skin wound repair. One is minimized mechanical stress: reduced swelling helps minimize volumetric expansion, which in turn lowers the risk of mechanical stress at the wound interface. Accordingly, the other is bioactive ion stimulation, sustained release of silicate ions promotes angiogenesis and ECM remodeling.

Vascularization is pivotal for wound regeneration, facilitating oxygen/nutrient supply [43]. Silicate ions from CS bioceramics are established inducers of endothelial cell (HUVEC) proliferation, migration, and tubulogenesis [44,45]. *In Vitro*, CS/AlgMA significantly enhanced the proliferation and migration of HUVECs (Figure 4a–e), indicating its potential to promote endothelial cell function. Concurrently, these cells orchestrate dermal reconstruction through collagen deposition, growth factor secretion and myofibroblast proliferation [46,47].

The 20%-CS/AlgMA formulation demonstrated superior *in vivo* performance for clinical translation potential, such as rapid epithelialization (96.0 ± 0.5% wound closure at day 14 (vs. 89.5 ± 1.2% in controls)), anti-inflammatory microenvironment, which reduced neutrophil infiltration and $CD68^+$ macrophages in H&E staining (Figure 5d) and mature collagen deposition (27.19 ± 4.38% collagen density at day 14 (Figure 5f)), indicating advanced remodeling. These outcomes stem from the 20%-CS/AlgMA's dual functionality. One is that AlgMA

matrix absorbs exudate without excessive swelling, and the other CS-derived ions continuously stimulate cellular processes critical for regeneration.

4. Conclusions

This study developed a dual-crosslinked CS/AlgMA to address wound management challenges. Methacrylation improved crosslinking density and reduced swelling by 70% versus conventional alginate hydrogels, which minimized secondary mechanical injury. Meanwhile, the optimized 20% CS/AlgMA showed sustained silicate/calcium ion release to stimulate the proliferation and migration of HUVECs *in vitro*, and *in vivo* assessments revealed CS/AlgMA may promote neovascularization and tissue remodeling, further accelerate wound closure (Day 14). Its 28-day degradation behavior suggests that this crosslinking strategy may be suitable for skin wounds repair period. However, this study has not evaluated long-term safety, efficacy in skin wounds, or anti-infection capacity. In addition, the relative contributions of the hydrogel matrix and ion release to the therapeutic effect could not be decoupled, physicochemically matched control hydrogels are therefore needed in future work. Future studies will employ established pressure ulcer, diabetic, or infected wound models to further verify its therapeutic potential in chronic wounds.

Supplementary Materials

The additional data and information can be downloaded at: https://media.sciltp.com/articles/others/261120153823 4723/RMD-26080060-SI.pdf. Figure S1: (**a**) Mannuronic acid (M sequence) on the left and glucuronic acid (G sequence) on the right. (**b**) Schematic diagram of AlgMA synthesis. Figure S2: (**a**) ^{1}H NMR spectra of AlgMA and Alg in D_2O; (**b**) area analysis of AlgMA hydrogen spectrum. Figure S3: Tensile stress-strain analysis of Alg-modified. Figure S4: Hydrophilic property test results of CS/AlgMA. Figure S5: Tensile stress-strain curve of CS/AlgMA. Figure S6: Ca^{2+} release profile. Table S1: Quantitative migration rate of HUVECs for 48 h (n = 5). Table S2: Quantitative collagen deposition by Masson's Trichrome. Ref. [48] has been cited in the Supplementary Material.

Author Contributions

C.S.: Conceptualization, investigation, methodology, data analysis, validation, writing—original draft; D.W.: Conceptualization, investigation, methodology, data analysis, validation; X.H.: Investigation, methodology, data analysis; Q.D.: Investigation, methodology, data analysis; L.T.: Investigation, methodology; S.W.: Conceptualization, supervision, project administration, writing—review & editing, funding acquisition; Z.D.: Conceptualization, supervision, project administration, writing—review & editing, funding acquisition. All authors have read and agreed to the published version of the manuscript.

Funding

This work was supported by the National Key R&D Program (2022YFA1105200), Sichuan Provincial Science and Technology Project (2025JDRC0057), Chengdu Technology Innovation R&D Project (2026-YF05-00306-SN), and Key Cultivation Project of Entrepreneurship Training Program for College Students in Chengdu University in 2025 (S202511079015X) and 2026 (202611079005X).

Institutional Review Board Statement

All procedures of Animal experiments were approved by the Institutional Animal Care and Use Committee (IACUC) of West China Hospital, Sichuan University (Protocol 20250422006) in compliance with NIH guidelines.

Informed Consent Statement

Informed consent was obtained from all subjects involved in the study.

Data Availability Statement

The data in the current study is available from the corresponding author on reasonable request.

Conflicts of Interest

The authors declare no conflict of interest.

Use of AI and AI-Assisted Technologies

No AI tools were utilized for this paper.

References

1. Svebak, S. The importance of skin area and gender in ticklishness. *Scand. J. Psychol.* **2021**, *62*, 683–688. https://doi.org/10.1111/sjop.12756.
2. Mathes, S.H.; Ruffner, H.; Graf-Hausner, U. The use of skin models in drug development. *Adv. Drug Deliv. Rev.* **2014**, *69–70*, 81–102. https://doi.org/10.1016/j.addr.2013.12.006.
3. Shpichka, A.; Butnaru, D.; Bezrukov, E.A.; et al. Skin tissue regeneration for burn injury. *Stem Cell Res. Ther.* **2019**, *10*, 94. https://doi.org/10.1186/s13287-019-1203-3.
4. Niculescu, A.G.; Grumezescu, A.M. An Up-to-Date Review of Biomaterials Application in Wound Management. *Polymers* **2022**, *14*, 421. https://doi.org/10.3390/polym14030421.
5. Liang, Y.; He, J.; Guo, B. Functional Hydrogels as Wound Dressing to Enhance Wound Healing. *ACS Nano* **2021**, *15*, 12687–12722. https://doi.org/10.1021/acsnano.1c04206.
6. Qi, L.; Zhang, C.; Wang, B.; et al. Progress in Hydrogels for Skin Wound Repair. *Macromol. Biosci.* **2022**, *22*, 2100475. https://doi.org/10.1002/mabi.202100475.
7. Miron, A.; Giurcaneanu, C.; Mihai, M.M.; et al. Antimicrobial Biomaterials for Chronic Wound Care. *Pharmaceutics* **2023**, *15*, 1606. https://doi.org/10.3390/pharmaceutics15061606.
8. Sethuram, L.; Thomas, J.; Mukherjee, A.; et al. A review on contemporary nanomaterial-based therapeutics for the treatment of diabetic foot ulcers (DFUs) with special reference to the Indian scenario. *Nanoscale Adv.* **2022**, *4*, 2367–2398. https://doi.org/10.1039/d1na00859e.
9. Dart, A.; Bhave, M.; Kingshott, P. Antimicrobial Peptide-Based Electrospun Fibers for Wound Healing Applications. *Macromol. Biosci.* **2019**, *19*, 1800488. https://doi.org/10.1002/mabi.201800488.
10. Zhao, Y.; Song, S.; Ren, X.; et al. Supramolecular Adhesive Hydrogels for Tissue Engineering Applications. *Chem. Rev.* **2022**, *122*, 5604–5640. https://doi.org/10.1021/acs.chemrev.1c00815.
11. Ahmad Raus, R.; Wan Nawawi, W.M.F.; Nasaruddin, R.R. Alginate and alginate composites for biomedical applications. *Asian J. Pharm. Sci.* **2021**, *16*, 280–306. https://doi.org/10.1016/j.ajps.2020.10.001.
12. Lee, K.Y.; Mooney, D.J. Alginate: Properties and biomedical applications. *Prog. Polym. Sci.* **2012**, *37*, 106–126. https://doi.org/10.1016/j.progpolymsci.2011.06.003.
13. He, Y.; Li, Y.; Sun, Y.; et al. A double-network polysaccharide-based composite hydrogel for skin wound healing. *Carbohydr. Polym.* **2021**, *261*, 117870. https://doi.org/10.1016/j.carbpol.2021.117870. Correction in *Carbohydr. Polym.* **2025**, *354*, 123312. https://doi.org/10.1016/j.carbpol.2025.123312.
14. Li, L.; Scheiger, J.M.; Levkin, P.A. Design and Applications of Photoresponsive Hydrogels. *Adv. Mater.* **2019**, *31*, 1807333. https://doi.org/10.1002/adma.201807333.
15. Sun, J.; Xiao, L.; Li, B.; et al. Genetically Engineered Polypeptide Adhesive Coacervates for Surgical Applications. *Angew. Chem. Int. Ed.* **2021**, *60*, 23687–23694. https://doi.org/10.1002/anie.202100064.
16. Norahan, M.H.; Pedroza-González, S.C.; Sánchez-Salazar, M.G.; et al. Structural and biological engineering of 3D hydrogels for wound healing. *Bioact. Mater.* **2023**, *24*, 197–235. https://doi.org/10.1016/j.bioactmat.2022.11.019.
17. Potharaju, S.; Jaaz, Z.A. Development and Characterization of Antimicrobial Nanocoatings for Titanium Dental Implants to Prevent Peri-Implantitis and Improve Osseointegration. *SHIFAA* **2023**, *2023*, 10–18. https://doi.org/10.70470/shifaa/2023/002.
18. Yang, C.; Ma, H.; Wang, Z.; et al. 3D Printed Wesselsite Nanosheets Functionalized Scaffold Facilitates NIR-II Photothermal Therapy and Vascularized Bone Regeneration. *Adv. Sci.* **2021**, *8*, 2100894. https://doi.org/10.1002/advs.202100894.
19. Dong, C.; Yang, C.; Younis, M.R.; et al. Bioactive NIR-II Light-Responsive Shape Memory Composite Based on Cuprorivaite Nanosheets for Endometrial Regeneration. *Adv. Sci.* **2022**, *9*, 2102220. https://doi.org/10.1002/advs.202102220.
20. Kong, L.; Wu, Z.; Zhao, H.; et al. Bioactive Injectable Hydrogels Containing Desferrioxamine and Bioglass for Diabetic Wound Healing. *ACS Appl. Mater. Interfaces* **2018**, *10*, 30103–30114. https://doi.org/10.1021/acsami.8b09191.
21. Shen, P.; Chen, Y.; Luo, S.; et al. Applications of biomaterials for immunosuppression in tissue repair and regeneration. *Acta Biomater.* **2021**, *126*, 31–44. https://doi.org/10.1016/j.actbio.2021.03.019.
22. Yi, M.; Li, H.; Wang, X.; et al. Ion Therapy: A Novel Strategy for Acute Myocardial Infarction. *Adv. Sci.* **2019**, *6*, 1, 1801260. https://doi.org/10.1002/advs.201801260. Correction in *Adv. Sci.* **2020**, *7*, 2000544. https://doi.org/10.1002/advs.202000544.
23. Pina, S.; Oliveira, J.M.; Reis, R.L. Natural-Based Nanocomposites for Bone Tissue Engineering and Regenerative Medicine: A Review. *Adv. Mater.* **2015**, *27*, 1143–1169. https://doi.org/10.1002/adma.201403354.
24. Chou, A.I.; Nicoll, S.B. Characterization of photocrosslinked alginate hydrogels for nucleus pulposus cell encapsulation. *J. Biomed. Mater. Res. Part A* **2009**, *91A*, 187–194. https://doi.org/10.1002/jbm.a.32191.

25. Zhang, Y.; Li, Y.; Liu, W. Dipole–Dipole and H-Bonding Interactions Significantly Enhance the Multifaceted Mechanical Properties of Thermoresponsive Shape Memory Hydrogels. *Adv. Funct. Mater.* **2015**, *25*, 471–480. https://doi.org/10.1002/adfm.201401989.
26. Soeriyadi, A.H.; Trouillet, V.; Bennet, F.; et al. A detailed surface analytical study of degradation processes in (meth)acrylic polymers. *J. Polym. Sci. Part A Polym. Chem.* **2012**, *50*, 1801–1811. https://doi.org/10.1002/pola.25947.
27. Wei, W.; Liu, W.; Kang, H.; et al. A One-Stone-Two-Birds Strategy for Osteochondral Regeneration Based on a 3D Printable Biomimetic Scaffold with Kartogenin Biochemical Stimuli Gradient. *Adv. Healthc. Mater.* **2023**, *12*, 2300108. https://doi.org/10.1002/adhm.202300108.
28. Hennink, W.E.; van Nostrum, C.F. Novel crosslinking methods to design hydrogels. *Adv. Drug Deliv. Rev.* **2012**, *64*, 223–236. https://doi.org/10.1016/j.addr.2012.09.009.
29. Liu, J.; Zheng, H.; Poh, P.; et al. Hydrogels for Engineering of Perfusable Vascular Networks. *Int. J. Mol. Sci.* **2015**, *16*, 15997–16016. https://doi.org/10.3390/ijms160715997.
30. Baker, M.J.; Trevisan, J.; Bassan, P.; et al. Using Fourier transform IR spectroscopy to analyze biological materials. *Nat. Protoc.* **2014**, *9*, 1771–1791. https://doi.org/10.1038/nprot.2014.110.
31. Makarova, A.O.; Derkach, S.R.; Khair, T.; et al. Ion-Induced Polysaccharide Gelation: Peculiarities of Alginate Egg-Box Association with Different Divalent Cations. *Polymers* **2023**, *15*, 1243. https://doi.org/10.3390/polym15051243.
32. Cui, H.; Wang, W.; Shi, L.; et al. Superwettable Surface Engineering in Controlling Cell Adhesion for Emerging Bioapplications. *Small Methods* **2020**, *4*, 12. https://doi.org/10.1002/smtd.202000573.
33. Kharaziha, M.; Baidya, A.; Annabi, N. Rational Design of Immunomodulatory Hydrogels for Chronic Wound Healing. *Adv. Mater.* **2021**, *33*, 2100176. https://doi.org/10.1002/adma.202100176.
34. Pauty, J.; Usuba, R.; Cheng, I.G.; et al. A Vascular Endothelial Growth Factor-Dependent Sprouting Angiogenesis Assay Based on an *In Vitro* Human Blood Vessel Model for the Study of Anti-Angiogenic Drugs. *EBioMedicine* **2018**, *27*, 225–236. https://doi.org/10.1016/j.ebiom.2017.12.014. Correction in *EBioMedicine* **2018**, *29*, 196. https://doi.org/10.1016/j.ebiom.2018.01.042.
35. Frykberg, R.G.; Banks, J. Challenges in the Treatment of Chronic Wounds. *Adv. Wound Care* **2015**, *4*, 560–582. https://doi.org/10.1089/wound.2015.0635.
36. Fonder, M.A.; Lazarus, G.S.; Cowan, D.A.; et al. Treating the chronic wound: A practical approach to the care of nonhealing wounds and wound care dressings. *J. Am. Acad. Dermatol.* **2008**, *58*, 185–206. https://doi.org/10.1016/j.jaad.2007.08.048.
37. Han, G.; Ceilley, R. Chronic Wound Healing: A Review of Current Management and Treatments. *Adv. Ther.* **2017**, *34*, 599–610. https://doi.org/10.1007/s12325-017-0478-y.
38. Ferreira, M.O.G.; de Lima, I.S.; Morais, A.Í.S.; et al. Chitosan associated with chlorhexidine in gel form: Synthesis, characterization and healing wounds applications. *J. Drug Deliv. Sci. Technol.* **2019**, *49*, 375–382. https://doi.org/10.1016/j.jddst.2018.12.003.
39. Okur, M.E.; Karantas, I.D.; Şenyiğit, Z.; et al. Recent trends on wound management: New therapeutic choices based on polymeric carriers. *Asian J. Pharm. Sci.* **2020**, *15*, 661–684. https://doi.org/10.1016/j.ajps.2019.11.008.
40. Farahani, M.; Shafiee, A. Wound Healing: From Passive to Smart Dressings. *Adv. Healthc. Mater.* **2021**, *10*, 2100477. https://doi.org/10.1002/adhm.202100477.
41. Chen, X.; Zhang, J.; Chen, G.; et al. Hydrogel Bioadhesives with Extreme Acid-Tolerance for Gastric Perforation Repairing. *Adv. Funct. Mater.* **2022**, *32*, 2202285. https://doi.org/10.1002/adfm.202202285.
42. Tottoli, E.M.; Dorati, R.; Genta, I.; et al. Skin Wound Healing Process and New Emerging Technologies for Skin Wound Care and Regeneration. *Pharmaceutics* **2020**, *12*, 735. https://doi.org/10.3390/pharmaceutics12080735.
43. Eming, S.; Brachvogel, B.; Odorisio, T.; et al. Regulation of angiogenesis: Wound healing as a model. *Prog. Histochem. Cytochem.* **2007**, *42*, 115–170. https://doi.org/10.1016/j.proghi.2007.06.001.
44. Han, Y.; Zeng, Q.; Li, H.; et al. The calcium silicate/alginate composite: Preparation and evaluation of its behavior as bioactive injectable hydrogels. *Acta Biomater.* **2013**, *9*, 9107–9117. https://doi.org/10.1016/j.actbio.2013.06.022.
45. Zhang, J.; Zeng, Z.; Chen, Y.; et al. 3D-printed GelMA/$CaSiO_3$ composite hydrogel scaffold for vascularized adipose tissue restoration. *Regen. Biomater.* **2023**, *10*, rbad049. https://doi.org/10.1093/rb/rbad049.
46. Bielefeld, K.A.; Amini-Nik, S.; Alman, B.A. Cutaneous wound healing: Recruiting developmental pathways for regeneration. *Cell. Mol. Life Sci.* **2013**, *70*, 2059–2081. https://doi.org/10.1007/s00018-012-1152-9.
47. Witte, R.P.; Kao, W.J. Keratinocyte-fibroblast paracrine interaction: The effects of substrate and culture condition. *Biomaterials* **2005**, *26*, 3673–3682. https://doi.org/10.1016/j.biomaterials.2004.09.054.
48. Kapishon, V.; Whitney, R.A.; Champagne, P.; et al. Polymerization Induced Self-Assembly of Alginate Based Amphiphilic Graft Copolymers Synthesized by Single Electron Transfer Living Radical Polymerization. *Biomacromolecules* **2015**, *16*, 2040–2048. https://doi.org/10.1021/acs.biomac.5b00470.